

On the potential of a new IVUS elasticity modulus imaging approach for detecting vulnerable atherosclerotic coronary plaques: *in vitro* vessel phantom study

Simon Le Floc^{h1,2}, Guy Cloutier^{2,3,7}, Gérard Finet⁴, Philippe Tracqui¹, Roderic I Pettigrew⁵ and Jacques Ohayon^{1,5,6,7}

¹ Laboratory TIMC-DynaCell, UJF, CNRS UMR 5525, In³S, Grenoble, France

² Laboratory of Biorheology and Medical Ultrasonics, Research Center, University of Montreal Hospital (CRCHUM), Montréal, Québec, Canada

³ Department of Radiology, Radio-Oncology and Nuclear Medicine, and Institute of Biomedical Engineering, University of Montreal, Montréal, Québec, Canada

⁴ Department of Hemodynamics and Interventional Cardiology, Hospices Civils de Lyon and Claude Bernard University Lyon 1, INSERM Unit 886, Lyon, France

⁵ Laboratory of Integrative Cardiovascular Imaging Science, National Institute of Diabetes Digestive and Kidney Diseases, National Institutes of Health, Bethesda, MD, USA

⁶ University of Savoie, Engineering School Polytech, Savoie, France

E-mail: Guy.Cloutier@umontreal.ca and Jacques.Ohayon@imag.fr

Received 27 April 2010, in final form 26 July 2010

Published 8 September 2010

Online at stacks.iop.org/PMB/55/5701

Abstract

Peak cap stress amplitude is recognized as a good indicator of vulnerable plaque (VP) rupture. However, such stress evaluation strongly relies on a precise, but still lacking, knowledge of the mechanical properties exhibited by the plaque components. As a first response to this limitation, our group recently developed, in a previous theoretical study, an original approach, called iMOD (imaging modulography), which reconstructs elasticity maps (or modulograms) of atheroma plaques from the estimation of strain fields. In the present *in vitro* experimental study, conducted on polyvinyl alcohol cryogel arterial phantoms, we investigate the benefit of coupling the iMOD procedure with the acquisition of intravascular ultrasound (IVUS) measurements for detection of VP. Our results show that the combined iMOD-IVUS strategy: (1) successfully detected and quantified soft inclusion contours with high positive predictive and sensitivity values of $89.7 \pm 3.9\%$ and $81.5 \pm 8.8\%$, respectively, (2) estimated reasonably cap thicknesses larger than $\sim 300 \mu\text{m}$, but underestimated thinner caps, and (3) quantified satisfactorily Young's modulus of hard medium (mean value of $109.7 \pm 23.7 \text{ kPa}$ instead of $145.4 \pm 31.8 \text{ kPa}$), but overestimated the stiffness of soft inclusions (mean Young's moduli of $31.4 \pm 9.7 \text{ kPa}$ instead of

⁷ Authors to whom any correspondence should be addressed.

17.6 ± 3.4 kPa). All together, these results demonstrate a promising benefit of the new iMOD-IVUS clinical imaging method for *in vivo* VP detection.

(Some figures in this article are in colour only in the electronic version)

1. Introduction

The major cause of acute coronary syndrome is the result of atherosclerotic plaque rupture (Fuster *et al* 2005, Virmani *et al* 2000, Naghavi *et al* 2003). The thin-cap fibroatheroma (TCFA) is the precursor lesion that once ruptured, may lead to the formation of a thrombus obstructing daughter coronary branches, causing an acute syndrome and the patient death (Virmani *et al* 2006). Histological, biomechanical and clinical studies showed that morphological parameters identifying a vulnerable plaque (VP) include the presence of a large necrotic core and a thin fibrous cap infiltrated by macrophages, which can be further complicated by accumulated calcium nodules (Vengrenyuk *et al* 2006).

Several clinical imaging techniques are in development to detect VPs, including intravascular ultrasound (IVUS) (Carlier and Tanaka 2006, Rioufol *et al* 2002), optical coherence tomography (OCT) (Jang *et al* 2002, Kubo *et al* 2007, Tearney *et al* 2008), computed tomography (Fayad *et al* 2002), and magnetic resonance imaging (MRI) (Briley-Saebo *et al* 2007). However, prediction of plaque rupture based on imaging features of morphology and composition, still provide rather imprecise and insufficient predictors of risk (Loree *et al* 1992, Shah 1998, Ohayon *et al* 2008). The challenge for such vascular imaging methods is that the prediction of the coronary plaque rupture also requires a precise knowledge of the mechanical properties of the arterial wall and plaque components at any given stage of plaque growth and remodeling (Cheng *et al* 1993, Finet *et al* 2004, Ohayon *et al* 2001). Indeed, such knowledge may allow a precise evaluation of the TCFA peak stress amplitude, which appears to be a good biomechanical predictor of plaque rupture, based on simulation results (Loree *et al* 1992, Ohayon *et al* 2008).

Reconstruction of plaque elasticity is difficult since atherosclerotic lesions are highly heterogeneous; nevertheless, this is a challenge that has been approached by a rather large diversity of methods (Vorp *et al* 1995, Soualmi *et al* 1997, Vonesh *et al* 1997, Beattie *et al* 1998, Chandran *et al* 2003, Khalil *et al* 2006, Cimrman and Rohan 2010, Pazos *et al* 2010). Generally, elasticity maps (or modulograms) are computed with *a priori* knowledge on the strain field (or elastogram) of atheromatous plaques and used either direct (Kim *et al* 2004, Kanai *et al* 2003) or iterative approaches (Fehrenbach *et al* 2006, Karimi *et al* 2008, Baldewsing *et al* 2008) to minimize the error between measured and computed plaque strains.

However, we hypothesize that the main issue for improving such methods does not mostly rely on the optimization algorithm itself, but rather on the pre-conditioning of the algorithm based on the best estimation of plaque component boundaries. Following this spirit, Baldewsing *et al* (2006) developed an elegant parametric finite element model (PFEM) to assess modulograms of VPs. However, one major limitation of their method is the use of a superposition technique, which ignores mechanical interactions between inclusions. To overcome such limitation, our group recently proposed both an original pre-conditioning step to extract the plaque morphology and a new approach combining a dynamic watershed segmentation (DWS) method with an optimization procedure (named iMOD for imaging modulography) to highlight modulograms of atherosclerotic lesions (Le Floc'h *et al* 2009).

The complete mathematical description of iMOD, which is based on the continuum mechanics theory prescribing the strain field, can be found in the above-mentioned study

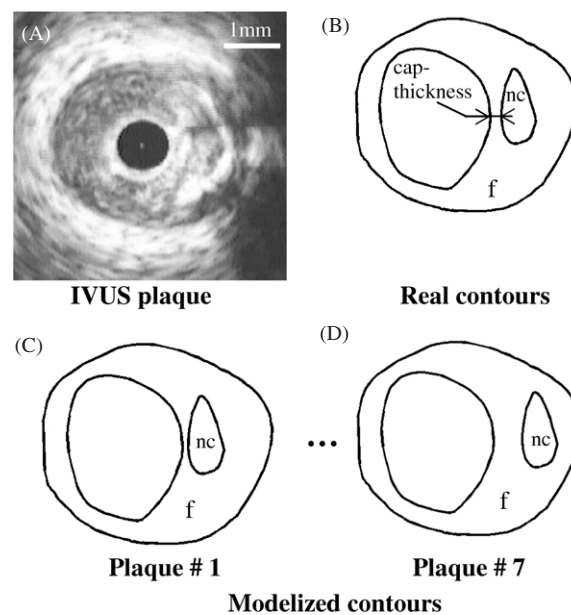


Figure 1. (A) An *in vivo* IVUS image and (B) real contours of this vulnerable coronary plaque with cap thickness = $119 \mu\text{m}$ and necrotic core area = 0.782 mm^2 . Six idealized VP models were manually traced by varying the initial fibrous cap thickness ($\text{Cap}_{\text{thick}}$) from $59 \mu\text{m}$ to $598 \mu\text{m}$ ($\text{Cap}_{\text{thick}}$ of plaques 1 to 7 are equal to 59, 119, 179, 239, 299, 448 and $598 \mu\text{m}$, respectively). The necrotic core shape and area were kept the same for all plaques. f: fibrosis; nc: necrotic core.

(Le Floc'h *et al* 2009). However so far, iMOD has neither been tested nor validated with real IVUS data. Therefore, the present numerical and experimental study was designed to investigate performances of this new promising plaque elasticity reconstruction algorithm iMOD. We first assessed iMOD for predicting plaque vulnerability based on relevant clinical indices (such as TCFA thickness, necrotic core size and area) by using mimicked IVUS images of coronary lesions simulated with Field II. In a second step, *in vitro* polyvinyl alcohol cryogel (PVA-C) vascular phantom experiments were conducted with IVUS acquisitions to investigate the accuracy of modulograms. In conclusion of this study, we discuss the potential of iMOD to extract modulographic images *in vivo*.

2. Material and methods

2.1. Simulation of intravascular B-mode ultrasound images

2.1.1. Plaque morphology. A non-ruptured VP morphology was obtained from a patient who underwent coronary IVUS at the Lyon Cardiology Hospital (Lyon, France) after a first acute coronary syndrome with troponin I elevation. From manually segmented contours of this vulnerable plaque, six additional cross-sectional plaque morphologies were designed by varying the cap thickness from $60 \mu\text{m}$ (i.e. instable VP) to $600 \mu\text{m}$ (i.e. stable VP) (figure 1). These models were used to investigate the performance of the proposed algorithm when approximating the plaque morphology and modulogram reconstructions.

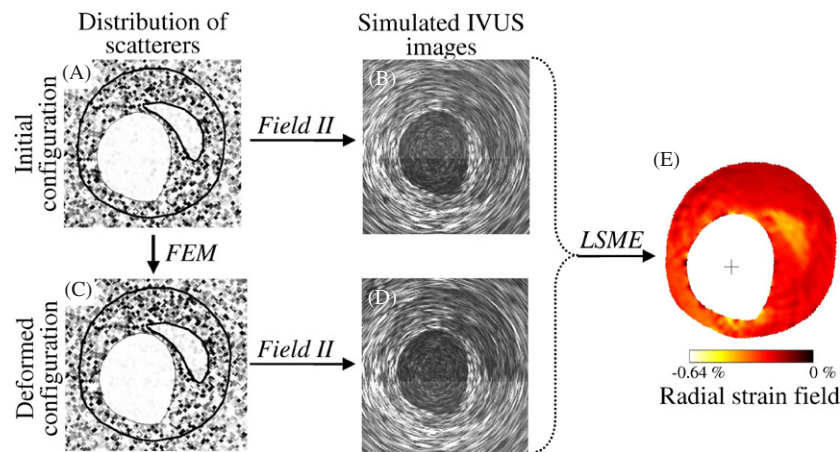


Figure 2. Schematic description of the successive steps performed to compute the radial strain map based on simulated IVUS B-mode images generated with the open source Field II code. FEM: finite element method; LSME: Lagrangian speckle model estimator.

2.2. Simulation of ultrasound images

Figure 2 illustrates the method used to simulate ultrasound images. Blood, arterial wall, plaque components and non-arterial surrounding tissue were characterized by their IVUS echogenicity aspect. In our simulations, echogenicities of the different segmented regions were mimicked by varying the acoustic scattering amplitude. This amplitude was determined by a Gaussian distribution, whose standard deviation (mean equal to zero) was adjusted according to the diffusive power of each tissue (Ramirez *et al* 2004). The relative acoustic scatterer amplitudes of blood, necrotic core and fibrosis were equal to 10, 15 and 60%, respectively, with an arbitrarily reference value of 100% for the relative acoustic amplitude of calcium. Scatterers were randomly distributed within each constituent of the atherosclerotic plaque. First, a pre-loading IVUS image corresponding to the initial state at an arbitrarily blood pressure was reconstructed. Then, a pressure step was applied and the resulting displacement field computed by finite element (FE) modeling was used to track the location of scatterers in the deformed configuration. A post-loading IVUS image was then generated with Field II (Jensen and Svendsen 1992) using the deformed configuration of scatterers. Since scatterers were randomly distributed, 32 distinct scatterer distributions were used to perform Field II computations to simulate ultrasound images from the 7 pairs of post- and pre-loading configurations. Thus, 7×32 pre-loaded and 7×32 post-loaded ultrasound images were simulated with Field II. The Field II open source software was modified to simulate IVUS images, as described by Fromageau (2003) and Ramirez *et al* (2004). The ultrasound intravascular probe—located at the centroid of the lumen—was simulated as a single rotating piezo-electric element of $600 \mu\text{m}$ in diameter, incremented by 1.4° to obtain each simulated radio-frequency (RF) line (256 lines per image). The central emission frequency was set to 20 MHz and the echo signal was sampled at 100 MHz. Note that these values also correspond to the parameters of the IVUS acquisition system used for the *in vitro* phantom experiments.

2.2.1. Finite element model. Static FE computations were performed on the VP morphologies (figure 2) using the COMSOL Multiphysics software (Structural Mechanics

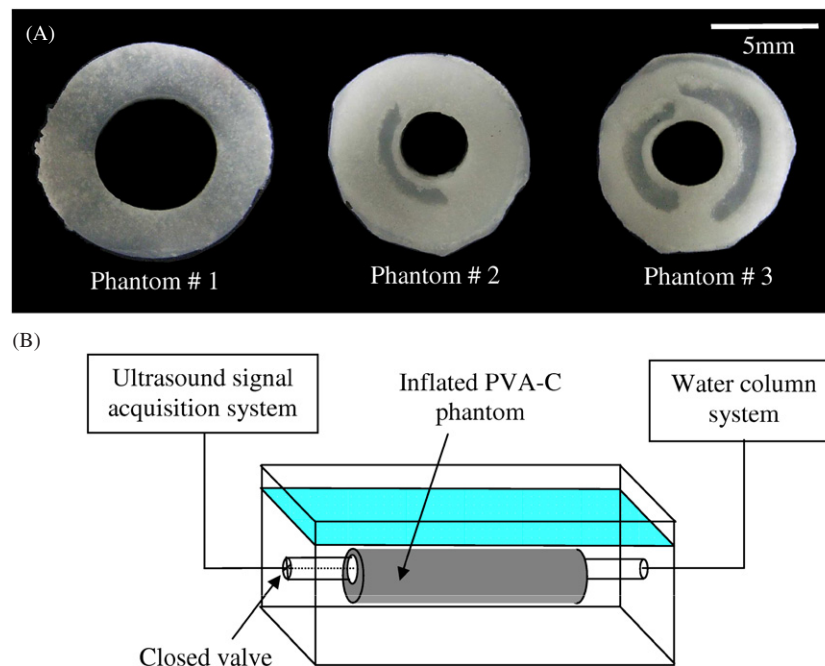


Figure 3. (A) Sections of the three PVA cryogel phantoms. (B) Schematic draw of the experimental setup composed of a water tank, the PVA-C phantom, a water column system to pressurize the phantom and the ultrasound acquisition system.

Module, COMSOL, version 3.5.0.608, COMSOL Inc., Grenoble, France). Plaque geometries were meshed with approximately 15 000 6-node triangular elements. The FE models were solved under the assumption of plane strain and a blood pressure step of 0.49 kPa (or 3.7 mmHg), which corresponds to a realistic pressure gradient occurring between two successive IVUS images recorded during the systolic phase. On the external contour of the artery, free boundary condition was assumed. The fibrosis and soft necrotic core were modeled as isotropic quasi-incompressible media (Poisson's ratio = 0.49) with Young's moduli $E_{\text{fibrosis}} = 600$ kPa and $E_{\text{core}} = 10$ kPa, respectively (Finet *et al* 2004).

2.3. Experimental *in vitro* study with PVA-C vessel phantoms

2.3.1. Phantom preparation. The vessel phantoms were made with the PVA-C tissue-mimicking material. The stiffness of the PVA-C increases with the number of freeze-thaw cycles. The preparation protocol followed the methodology described in Fromageau *et al* (2007). The solution used had a concentration of 10% by weight of polyvinyl alcohol dissolved in pure water and ethanol homopolymer. The weight by weight percentage of added Sigmacell particles used as acoustic scatterers (Sigmacell Cellulose, type 50, Sigma Chemical, St Louis, MO, USA) was 3%. Solidification and polymerization of PVA-C samples were induced by one to six freezing-thawing cycles, using a specifically designed temperature-controlled chamber. A freeze-thaw rate cycle lasted 24 h, and the freeze-thaw temperature and rate of change were ± 20 °C and ± 0.2 °C min⁻¹, respectively. The durations of freeze and thaw stages were the same and equal to 3h20.

Three cylindrical vessel phantoms were made using tubes and rods of different diameters, as described in figure 3(A) of Maurice *et al* (2005b) (see figure 3(A) of the current study).

One homogeneous vessel phantom was made by performing one freeze-thaw cycle; for the two composite phantoms, the vessel wall experienced six freeze-thaw cycles and inclusions mimicking soft necrotic cores were filled with PVA-C before the last cycle (inclusions thus underwent one freeze-thaw cycle only). Note that the cavities of the soft necrotic cores could be filled with PVA-C by injection only after removing the corresponding parts of the mould. Heterogeneous phantoms with bad adherence at the interface of the soft inclusion with the surrounding hard material were excluded from our experiments.

2.3.2. Mechanical characterization of PVA-C media. Both linear and nonlinear mechanical behaviors of the soft and hard PVA-C media, used to fabricate vessel phantoms, were investigated. Cylindrical samples were made at the same time within the same temperature chamber, with the same PVA-C solution as the arterial phantoms with one and six freeze-thaw cycles. A Poisson's ratio of 0.5 (i.e. incompressible medium) was considered to derive Young's moduli of these PVA-C gel samples. The behaviors of the two PVA-C media were investigated by performing compression tests on the cylindrical samples using a dynamic mechanical testing instrument (GABO Eplexor, Ahlden, Germany, load cell of 25 N, sensor sensitivity of 10^{-4} at full range).

2.3.3. Experimental IVUS setup. The arterial phantoms were mounted in a circuit and quasi-statically pressurized with a water column, as shown in figure 3(B). Water temperature was stabilized at $25\text{ }^{\circ}\text{C} \pm 1\text{ }^{\circ}\text{C}$ before each experiment. Cross-sectional RF images were acquired at different pressure steps with an IVUS scanner (model In-Vision Gold, Volcano Therapeutics, Rancho Cordova, CA, USA) equipped with a 20 MHz IVUS catheter. RF images were digitalized at 100 MHz with an external data acquisition system (model Remora, Volcano Therapeutics). The pressure gradient step was set to 0.25 kPa (i.e. 25 mm of water height) and 0.5 kPa (i.e. 50 mm of water height) for the homogeneous and heterogeneous phantoms, respectively. For each vessel phantom, ten successive pressure gradient steps were imposed (corresponding to an increase of pressure from 0 kPa to 2.5 kPa and from 0 kPa to 5 kPa for both phantoms, respectively) to investigate how the nonlinear PVA-C behavior could be measured from successive elasticity map reconstructions.

2.4. Elasticity map reconstruction

2.4.1. Intravascular elastography. As displayed in figure 2, the Lagrangian speckle model estimator (LSME) (Maurice *et al* 2004) was used to compute the radial strain field of both simulated and experimental RF images. The first step of this method consisted in a local rigid registration on overlapping sub-windows (measurement windows—MWs) that allowed compensating for potential translation movements using 2D cross-correlation analysis. In a second step, a nonlinear minimization problem based on the optical flow equations was solved for each MW to assess the 2D deformation matrix (Maurice *et al* 2004). The radial length and circumferential width of the MWs and the step size in both directions (corresponding to radial and circumferential overlaps) were respectively fixed to 201 pixels (approximately 1.5 mm), 21 pixels (approximately 28°), 5 and 2 pixels (approximately 90% MW overlaps). Such values optimized the performances of the LSME algorithm when ultrasound data are acquired at 20 MHz with a sampling frequency of 100 MHz (Maurice *et al* 2007).

2.4.2. Segmentation of the luminal and external PVA-C vessel contours. The reconstructed B-mode images were segmented to detect the internal and external borders of each cross-section using an algorithm based on a fast-marching model combining region and contour

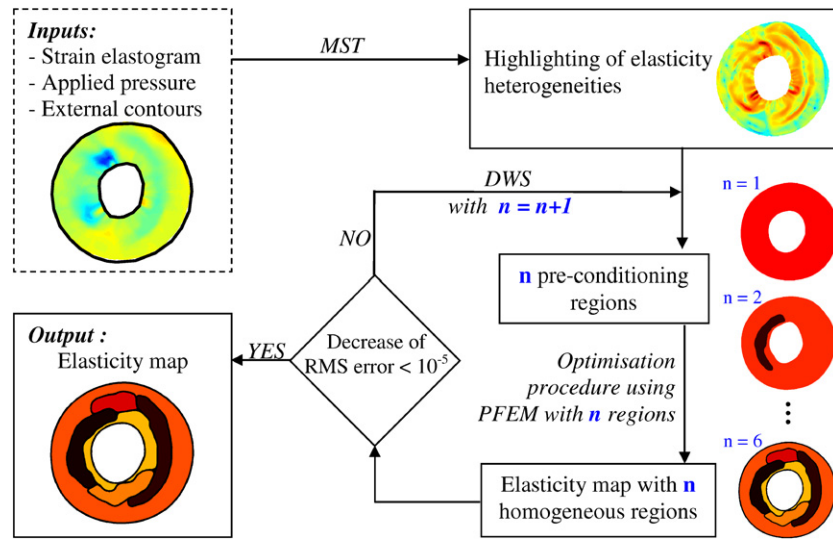


Figure 4. Schematic description of the successive reconstruction steps performed in the modulography algorithm iMOD. Modified Sumi's transform (MST) is first used to highlight the borders of the mechanical heterogeneities based on the estimated radial strain field. A parametric finite element model (PFEM) together with an optimization procedure is used to estimate intraplaque Young's moduli. The optimization procedure stops if the decrease of the root mean square (RMS) error becomes smaller than a given threshold value. DWS: dynamic watershed segmentation procedure.

information (Roy Cardinal *et al* 2006). These contours were used to reconstruct the spatial intraplaque elasticity map with the parametric FE iMOD model described next.

2.4.3. Arterial wall elasticity reconstruction algorithm. Figure 4 schematizes the successive steps performed by the proposed iMOD algorithm to identify the elasticity map from the radial strain field. The theoretical framework of this method has been described earlier (Le Floc'h *et al* 2009). Briefly, by using a gradient elasticity approach and by extending the method of Sumi and Nakayama (1998), originally proposed under the plane stress condition, to the plane strain condition, we deduced the following function dW that was proposed to extract intraplaque mechanical heterogeneities:

$$dW = -\frac{1}{\varepsilon_{rr}} \left(\frac{\partial \varepsilon_{rr}}{\partial r} + \frac{2\varepsilon_{rr}}{r} \right) dr - \frac{1}{\varepsilon_{rr}} \frac{\partial \varepsilon_{rr}}{\partial \theta} d\theta, \quad (1)$$

where ε_{rr} is the local intraplaque radial strain and (r, θ) describes the polar coordinates. This equation from here on is referred to as the modified Sumi's transform (MST).

The iMOD algorithm first consisted in computing the intraplaque spatial distribution of dW amplitude, a term very sensitive to the spatial derivative of Young's modulus. Second, based on the resulting MST-field, a DWS coupled with an optimization procedure was applied to obtain the elasticity map. The DWS procedure was applied to extract plaque mechanical heterogeneities called 'pre-conditioning regions'. Assuming that each region had a uniform stiffness, we derived Young's moduli of these pre-conditioning regions by running an optimization procedure that minimized the root mean squared (RMS) error between the computed radial PFEM and the estimated LSME radial strain field. The watershed (Watershed function, Imaging Tool Box, MATLAB, version 7.6., the MathWorks, Natick, MA, USA)

and minimization procedures (Optimization Lab Module, COMSOL, version 3.5, COMSOL Inc., Grenoble, France) were repeated with an increasing number of pre-conditioning regions in order to take into account smaller heterogeneity sizes. We assumed that a satisfactory solution was reached when the change of the RMS error between two successive iterations became lower than a threshold of 10^{-5} . A sequential quadratic programming algorithm with a numerical estimation of the gradient by the adjoint method (Gill *et al* 2005) was used for the optimization procedure. Note that the iMOD tool involves essentially three successive algorithmic procedures, namely (i) the computation (MST algorithm) of a pseudo-gradient elasticity map called the MST-field, (ii) the segmentation procedure (DWS algorithm) that makes use of the previous step results to extract the inclusions' contours, and finally (iii) the optimization procedure, which provides the estimated Young's moduli of the detected inclusions and surrounding tissue.

2.4.4. Geometric and elasticity reconstruction error measures. The accuracy of the plaque inclusion segmentation procedure was investigated based on the following two indices: (1) the positive predictive value (PPV), defined as the ratio between the 'true positive area' and the computed area, and (2) the sensitivity value (SV), defined as the ratio between the 'true positive area' and the real area. The 'true positive area' is the intersection between real and computed areas (Levner and Zhang 2007). Note that if the PPV and SV values are both equal to 100%, then the segmentation process reproduces the real contours. We also calculated the cap thickness (Cap_{thick}) and the necrotic core area ($Core_{area}$), which are important clinical indicators of plaque vulnerability.

For the *in vitro* study, the real cap thicknesses and inclusion areas of vessel phantoms were measured on five cross-sectional samples ($n = 5$) obtained by cutting, with a microtome equipped with a vibrating blade (HM 650 V Vibration Microtome, MICROM International GmbH, Robert-Bosch-Str. 49, D-69190 Walldorf); each IVUS explored PVA-C vessel segment in thin slices of $500 \mu m$ thickness. The mean cap thickness and the mean soft inclusion area values were used as reference outlines to compute the real Cap_{thick} and the real $Core_{area}$ metrics. However, the shape of the inclusions depends on the internal pressure applied to the vessel phantoms. Therefore, the reference outlines required for computing the PPV and SV index values cannot be extracted from the unloaded configuration of the cross-sectional samples. As an alternative, we took advantage of the high echogenicity gradient amplitude exhibited between one cycle (soft) and six cycle (hard) PVA-C media to extract such reference inclusion contours from manual segmentations of IVUS images.

3. Results

As illustrated earlier in figure 4, the iMOD algorithm iterates to define n pre-conditioning regions with specific mechanical elasticity moduli, depending on the plaque characteristics. For clarity reasons, simplified Young's modulus maps were computed by grouping together neighboring pre-conditioning regions with close stiffnesses. When applicable, for all plotted simplified modulograms, the mean stiffness ± 1 standard deviation were determined and reported for each merged contour.

3.1. Modulogram reconstruction of vulnerable plaques using simulated ultrasound images

Figure 5 illustrates the performance of the algorithm to detect soft inclusions and estimate cap thicknesses of vulnerable plaques with distinct Cap_{thick} equal to 119 , 299 and $598 \mu m$,

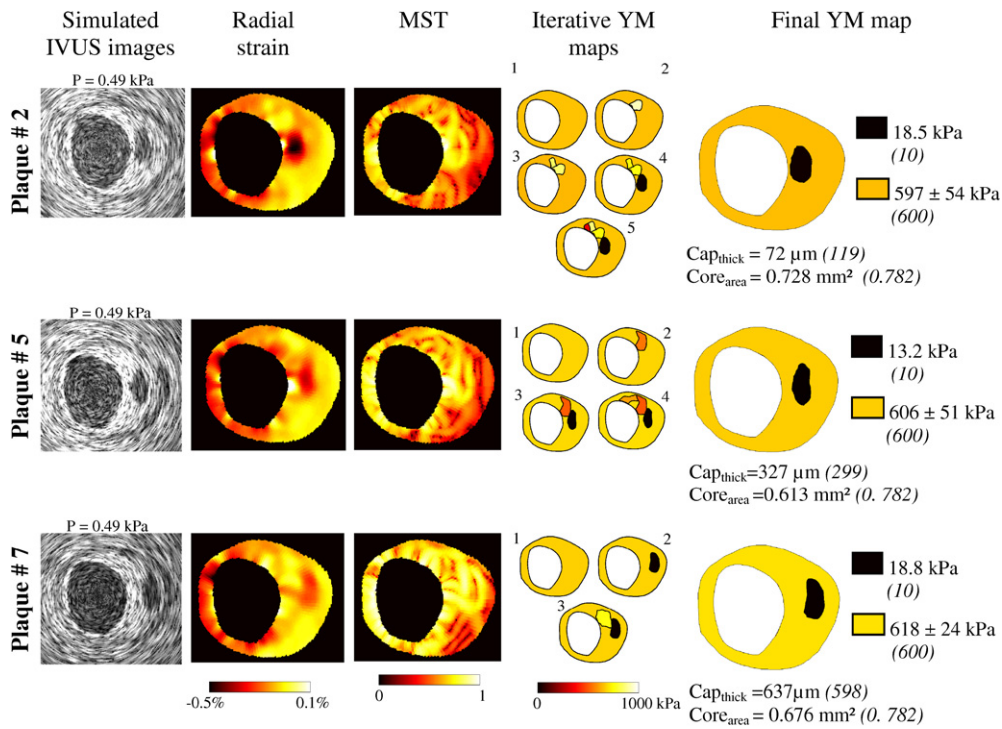


Figure 5. Performance of the method to obtain morphologies and modulograms from three simulated IVUS images of coronary vulnerable plaques. Column 1: simulated IVUS images; column 2: estimated radial strain fields obtained by using the Lagrangian speckle model estimator (LSME); column 3: spatial pseudo-gradient elasticity field resulting from the modified Sumi's transform (MST) procedure; column 4: evolution of Young's modulus (YM) map obtained during the iterative process combining the DWS and optimization procedures; column 5: simplified final Young's modulus maps and resulting estimations of cap thicknesses (Cap_{thick}) and necrotic core areas ($Core_{area}$). In parentheses are given the real values considered in the simulations (gold standard values).

respectively. For such simulations, only 5, 4 and 3 pre-conditioning regions were needed to detect the soft inclusion, respectively.

3.1.1. Validation of the segmentation procedure. Whatever the plaque considered (figure 1, plaques 1 to 7), the mean of the two segmentation performance indices PPV and SV were found to be, for the necrotic core, greater than 82.5% and 66.6%, respectively (table 1). These index values indicate a reasonable agreement between real and estimated necrotic core morphologies.

3.1.2. Quantification of cap thickness (Cap_{thick}) and core area ($Core_{area}$). Figure 6(A) shows the performance of the algorithm to estimate the Cap_{thick} of the seven vulnerable plaques considered (figure 1, plaques 1 to 7). In this evaluation, the label LSME-iMOD indicates the combined elastography and modulography method of the current study, whereas the label iMOD indicates computations realized with simulated instead of computed LSME strain fields (to determine which algorithm component LSME or iMOD contributed the most to the

Table 1. Analysis of the performance of the IVUS iMOD. Comparisons between computed and real plaque morphology indices and Young's moduli are presented. The accuracy of the approach was investigated by using simulated (Field II study) and real (*in vitro* study) IVUS images. S: soft inclusion area. PPV: predictive positive value. SV: sensitivity value. SD: standard deviation.

	Plaque morphology						Intraplaque Young's moduli (kPa)			
	S (mm ²)		PPV (%)	SV (%)	Cap thickness (μm)		Soft medium		Hard medium	
	Computed	Real			Computed	Real	Computed	Real	Computed	Real
<i>Field II study</i>										
Plaque 1	0.637 ± 0.088	0.782	90.2 ± 2.7	73.3 ± 9.1	22 ± 17	59	30.1 ± 10.8	10	592 ± 25	600
Plaque 2	0.697 ± 0.145	0.782	87.0 ± 7.8	76.3 ± 9.2	33 ± 26	119	48.1 ± 22.3	10	598 ± 31	600
Plaque 3	0.734 ± 0.130	0.782	85.5 ± 7.5	79.2 ± 8.5	73 ± 48	179	60.6 ± 31.5	10	603 ± 34	600
Plaque 4	0.709 ± 0.162	0.782	84.0 ± 9.0	74.4 ± 9.9	89 ± 82	239	69.0 ± 33.4	10	611 ± 37	600
Plaque 5	0.619 ± 0.094	0.782	87.6 ± 9.2	68.7 ± 8.8	223 ± 142	299	47.4 ± 41.0	10	614 ± 35	600
Plaque 6	0.683 ± 0.172	0.782	82.5 ± 12.2	69.7 ± 9.1	429 ± 159	448	52.6 ± 39.9	10	604 ± 30	600
Plaque 7	0.620 ± 0.139	0.782	85.4 ± 9.4	66.6 ± 10.4	606 ± 192	598	38.7 ± 40.4	10	604 ± 28	600
Mean ± SD	0.671 ± 0.140	0.782	86.0 ± 8.9	72.6 ± 10.1	–	–	49.5 ± 34.7	10	603.8 ± 31.9	600
<i>In vitro study</i>										
Phantom 1	–	–	–	–	–	–	29.2 ± 2.2	17.6 ± 3.4	–	–
Phantom 2	5.13 ± 0.12	4.70 ± 0.15	85.7 ± 3.3	92.3 ± 1.7	133 ± 67	281 ± 21	47.8 ± 8.0	17.6 ± 3.4	106.7 ± 14.2	145.4 ± 31.8
Phantom 3										
Core 1	5.16 ± 0.19	6.39 ± 0.38	91.9 ± 1.4	73.7 ± 5.9	134 ± 50	238 ± 29	20.0 ± 16.3	17.6 ± 3.4	112.4 ± 29.6	145.4 ± 31.8
Core 2	6.75 ± 0.35	7.81 ± 0.12	91.9 ± 2.7	78.7 ± 2.0	629 ± 103	612 ± 22	39.7 ± 12.5	17.6 ± 3.4	112.4 ± 29.6	145.4 ± 31.8
Mean ± SD	–	–	89.7 ± 3.9	81.5 ± 8.8	–	–	31.4 ± 9.7	17.6 ± 3.4	109.7 ± 23.7	145.4 ± 31.8

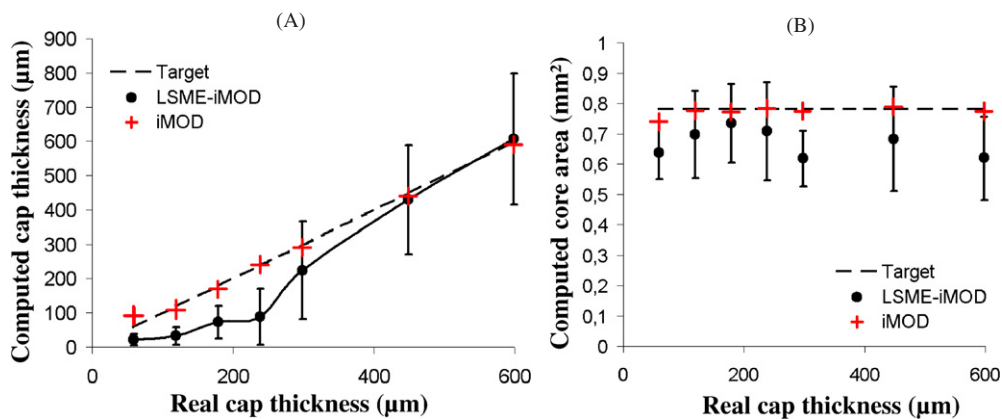


Figure 6. Performance of the elastography and modulography methods to estimate (A) cap thicknesses (Cap_{thick}) and (B) core areas ($Core_{area}$) of idealized vulnerable plaques with distinct Cap_{thick} equal to 59, 119, 179, 239, 299, 448 and 598 μm , respectively. The 'target' curve represents the real values. The 'LSME-iMOD' curve presents the results obtained with iMOD by using the elastogram computed with the LSME method. The 'iMOD' curve presents the results obtained with iMOD based on the exact elastogram computed by using the FE method.

reported biased measures of figure 6). When using LSME strain fields, cap thickness values were underestimated with relative errors ranging from -72.3% for plaque 2 with $Cap_{thick} = 59 \mu\text{m}$ to $+1.3\%$ for plaque 7 with $Cap_{thick} = 598 \mu\text{m}$ (also see table 1). The $Core_{area}$ were underestimated with a relative maximum error of -25.2% (figure 6(B)). However, variations of core areas as a function of simulated cap thicknesses were not significant ($p > 0.05$, based on a one-way analysis of variance, SigmaStat 3.5, Systat Software, Point Richmond, CA, USA). As indicated by results presented in figure 6, biased cap thickness and core area values are mainly attributed to the LSME performance.

3.1.3. Accuracy of computed modulograms. While Young's modulus of the fibrosis was reasonably identified (mean value of $603.8 \pm 31.9 \text{ kPa}$ instead of 600 kPa , table 1), the stiffness of the soft inclusion was overestimated (mean value of $49.5 \pm 34.7 \text{ kPa}$ instead of 10 kPa , table 1).

3.2. Modulogram reconstructions of PVA-C phantoms mimicking vulnerable plaques

Except when it is mentioned, each computed value was derived from the analysis conducted on the whole set of cross-sectional IVUS images acquired at each pressure step (ten pressure steps) and therefore represents the mean value \pm one standard deviation derived from these ten computations. Figure 7 exemplifies the performance of the combined LSME-iMOD algorithm to detect the morphology of the three PVA-C vessel phantoms mimicking a healthy vessel and vulnerable plaques. Elastograms (LSME radial strains), elasticity gradient fields (MST) and Young's modulus maps (modulograms) are presented.

3.2.1. Validation of the segmentation procedure. The accuracy of the segmentation was investigated on the basis of the three resulting inclusion contours computed for vessel phantoms 2 and 3 (figure 7). For both plaques, contours were estimated accurately since their positive

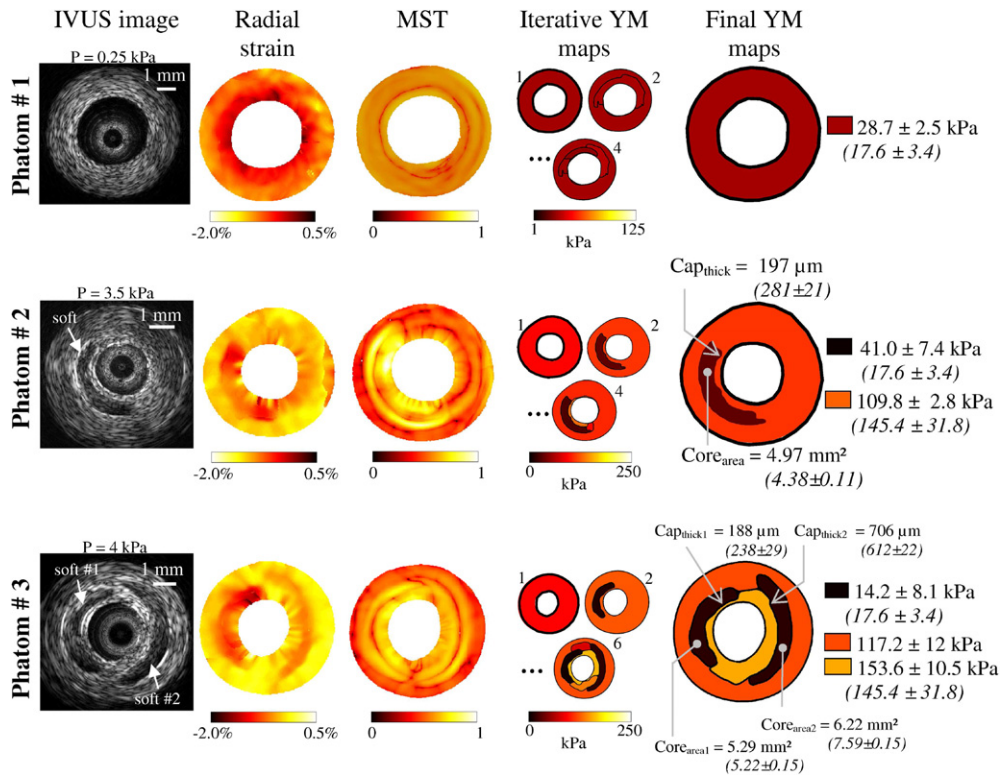


Figure 7. Performance of the LSME-iMOD method to detect soft inclusions using experimental IVUS images acquired on the three PVA-C phantoms presented in figure 3. Column 1: IVUS images; column 2: estimated radial strain fields obtained by using the Lagrangian speckle model estimator (LSME). Such strain fields result from pressure loading of 0.25, 3.5 and 4 kPa, for phantoms 1, 2 and 3, respectively; column 3: spatial pseudo-gradient elasticity field resulting from the modified Sumi's transform (MST) procedure; column 4: evolution of Young's modulus (YM) map obtained during the iterative procedure; column 5: final Young's modulus maps and resulting estimations of cap thicknesses (Cap_{thick}) and necrotic cores areas ($Core_{area}$). In parentheses are given the real values measured by histomorphometry (gold standard values).

PPV and SV mean values were found larger than 85.7% and 73.7%, respectively (table 1). Such results indicate that the $Core_{area}$ were satisfactorily estimated by this algorithm.

3.2.2. Quantification of the cap thickness (Cap_{thick}). For experiments performed with phantom 2, the Cap_{thick} was $133 \pm 67 \mu\text{m}$ (recall that figure 7 is one example with $Cap_{thick} = 197 \mu\text{m}$) whereas the measured mean reference Cap_{thick} equals $281 \pm 21 \mu\text{m}$. For the first and second soft inclusions of phantom 3, the mean Cap_{thick} were estimated at $134 \pm 50 \mu\text{m}$ and $629 \pm 103 \mu\text{m}$ while the measured mean references Cap_{thick} were $238 \pm 29 \mu\text{m}$ and $612 \pm 22 \mu\text{m}$, respectively (table 1). Our results thus show that the segmentation procedure underestimates (by a factor close to 2) the fibrous cap thickness for vulnerable plaques with Cap_{thick} smaller than approximately $300 \mu\text{m}$ (note that similar conclusions had been derived from the simulation study).

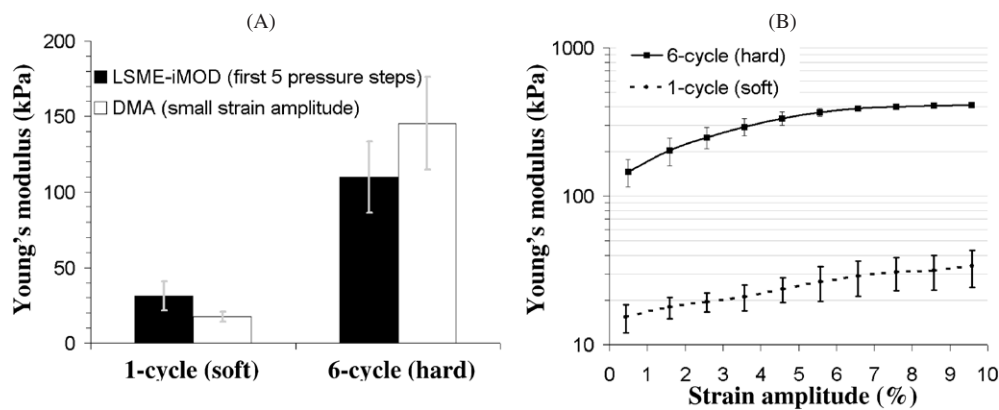


Figure 8. Measured and computed mechanical properties on the soft (one-cycle) and hard (six-cycle) PVA-C media. Young's moduli of these two PVA-C media were estimated by compression tests (DMA). (A) Comparison between mean Young's moduli computed by using the algorithm LSME-iMOD and those measured experimentally by DMA at low strain amplitude (compression < 2%). (B) The nonlinear mechanical behavior of the two PVA-C media was highlighted by performing a DMA test with compression strain varying between 1% and 10%, approximately.

3.2.3. Performance of the algorithm to characterize healthy vessels. The elasticity reconstruction performed on the homogeneous phantom 1, at the first pressure step, is presented in the top panel of figure 7. As expected at small pressure loading (i.e. under small strain solicitations), a quasi-uniform spatial Young's modulus distribution was found with a mean value of 28.7 ± 2.5 kPa. Moreover, the algorithm successfully reconstructed the elasticity maps with an optimum number of unknown Young's moduli of 4.

3.2.4. Performance of the algorithm to characterize complex vulnerable plaques. The IVUS elastograms and modulograms of the two complex phantoms mimicking vulnerable plaques were also successfully estimated (see figure 7, phantoms 2 and 3 for typical examples). For each pressure step, the combined LSME-iMOD procedure was able to detect the soft inclusions with a small number of pre-conditioning regions typically of 4 and 7 on average for phantoms 2 and 3, respectively.

3.2.5. Accuracy of computed modulograms: linear behavior. Comparisons between mean experimental values (measured with DMA at small strain amplitude < 2%) and computed Young's moduli for the one-cycle (soft material) and six-cycle (hard material) PVA-C media are presented in figure 8(A). Such comparisons were conducted by averaging computed Young's moduli of each medium (i.e. one cycle soft and six cycle hard) by considering only the first five modulograms obtained for each phantom. Based on paired *t*-tests (SigmaStat 3.5), DMA and modulography Young's moduli differed for both gels ($p < 0.05$). Note that only the first five pressure steps were considered to ensure small strain condition. The LSME-iMOD algorithm overestimated Young's moduli of soft inclusions (31.4 ± 9.7 kPa instead of 17.6 ± 3.4 kPa) and underestimated Young's moduli of the stiffer gel with a relative error close to -25% (109.7 ± 23.7 kPa instead of 145.4 ± 30.8 kPa).

3.2.6. Effect of the nonlinear mechanical behavior of PVA-C on modulograms. Because the mechanical properties of PVA-C media are nonlinear (see the DMA results in figure 8(B)), we

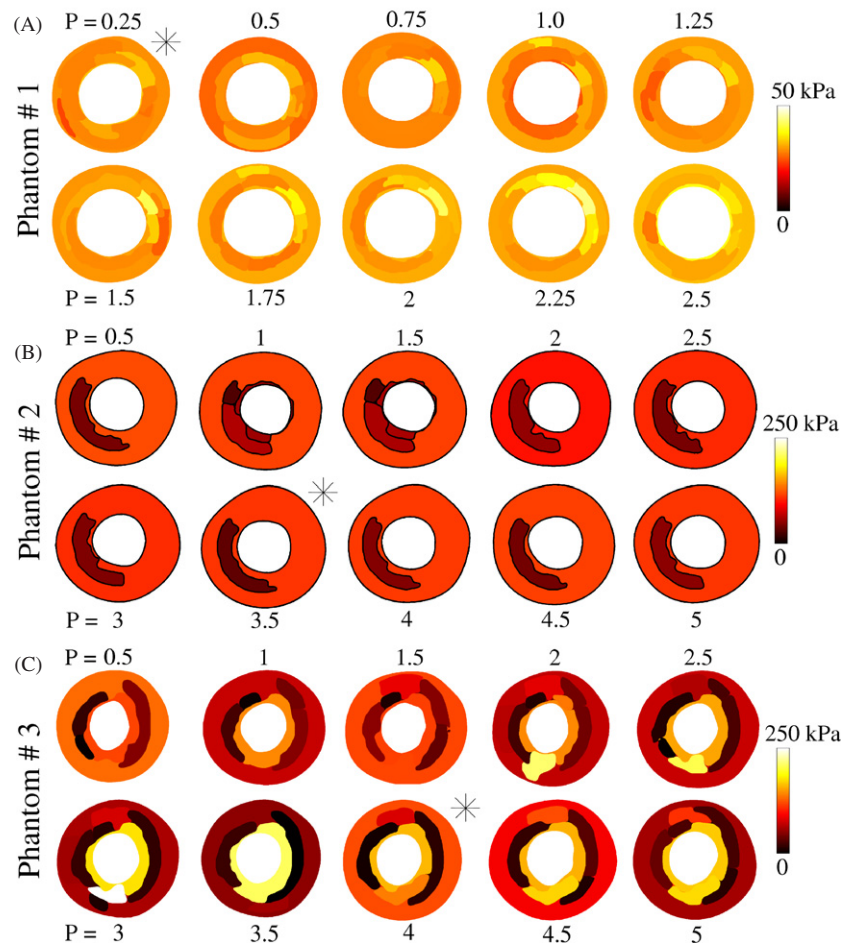


Figure 9. Young's modulus reconstructions considering the ten pressure steps for the three PVA-C phantoms: (A), (B) and (C) modulograms for phantoms 1, 2 and 3, respectively. The pressure P applied to the internal border of the phantoms is indicated in kPa. The asterisk indicates the pressure steps used for the experimental results presented in figure 7.

investigated the potential of the LSME-iMOD algorithm to sense the strain hardening of the gel by taking advantage of the series of cross-sectional IVUS images acquired for the three phantoms at each pressure step. Figure 9 summarizes the elasticity maps found for phantoms 1, 2 and 3. These modulograms were computed by considering the ten available sets of two successive IVUS images acquired during the pressure loading period. We quantified the increase of Young's moduli with strain from all computed modulograms presented in figure 9. For each phantom, we grouped all material points with regard to their strain amplitude. Six groups with 2% strain interval ranging approximately from 0% to 12% were considered and corresponding mean Young's moduli ± 1 standard deviations were computed (figure 10). The six-cycle hard medium of phantom 3, mimicking a VP with two soft inclusions, highlighted the strongest strain hardening effect with mean Young's moduli increasing from 114.7 ± 38.5 kPa for small strain (i.e. close to 1%) to 171.7 ± 15.3 kPa for large strain (i.e. close to

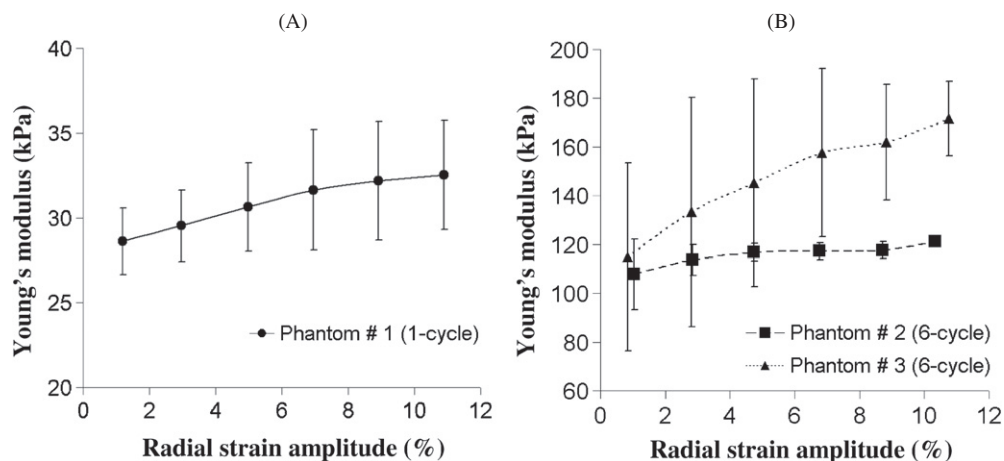


Figure 10. Nonlinear mechanical behavior of PVA-C media. The strain hardening effect was also demonstrated by using the LSME-iMOD algorithm, at each step during the pressure loading phase. The increase of the local Young's modulus with strain amplitude is observed for (A) the soft gel of phantom 1 and (B) the hard gel of phantoms 2 and 3.

12%) (figure 10(B)). Similar effects were also observed for phantom 1 mimicking a healthy vessel (figure 10(A)). The strain hardening was less important for phantom 2.

4. Discussion

Quantifying *in vivo* the mechanical properties of VP components at any given time of the remodeling process remains a major issue, as it could lead to the development of specific therapies for the prevention of acute coronary events (Libby 2001). Although intraplaque spatial strain distributions can be approximated and measured *in vivo* quite reasonably (de Korte *et al* 2002, Kim *et al* 2004, Wan *et al* 2001, Maurice *et al* 2005a), the determination of plaque component mechanical elasticity moduli, plaque inclusion boundaries and cap thickness remain difficult to assess for complex VP morphologies.

The main purpose of this work was to provide a robust and reliable image processing algorithm to detect and diagnose vulnerable plaques following an IVUS exam. Our original PFEM modulography approach, combining the strain estimator model LSME, the MST and the dynamic segmentation procedure (DSW), was successfully tested using both simulated and real IVUS images of plaque morphologies mimicking atherosclerotic lipid-rich lesions. The *in vitro* experiment conducted with a clinical IVUS acquisition system and performed on PVA-C arterial phantoms highlighted the potential and the robustness of the whole IVUS measurement procedure proposed to detect complex vulnerable plaques.

4.1. Necessity to use a priori information

It is essential to introduce *a priori* information to constrain the resolution of the inverse problem so that a unique elasticity reconstruction map solution could be extracted from the knowledge of the radial strain field (Baldewsing *et al* 2005, Barbone and Bamber 2002). By using a FE method and by performing a sensitivity analysis of the displacement field with regard to the mechanical properties of the FEs, Chandran *et al* (2003) identified equi-rigidity regions

before their iterative procedure in order to constrain their optimization algorithm. Other groups (Beattie *et al* 1998, Khalil *et al* 2006, Karimi *et al* 2008) extracted plaque morphology from direct segmentation of medical images. An interesting method using adaptive Bezier curves was developed by Baldewsing *et al* (2006) to take into account complex necrotic core geometries. Despite its robustness when applied to plaques with a unique inclusion, this approach would likely not be accurate enough to extract the elasticity map of a plaque embedding heterogeneous mechanical inclusions such as neighboring necrotic cores and/or calcium inclusions, thus preventing a good diagnosis of plaque vulnerability. More recently, Li *et al* (2008) developed a new PFEM driven by a split and merge iterative segmentation procedure. In their approach, the axial strain field was used to constrain the inverse problem by segmenting/merging the whole domain in regions so that the inverse problem becomes mathematically well defined to obtain a unique modulogram solution. Despite its robustness when applied to cancer tumor detection, this PFEM would have some limitations when applied to VP elasticity reconstruction. Indeed in the case of atherosclerotic plaques and due to the natural strain decay occurring from the lumen to the adventitia, this method would not be efficient enough to highlight accurately the plaque morphology and more particularly plaque heterogeneities far from the lumen. The strain decay phenomenon is illustrated in figure 5; the necrotic core with a predefined Young's modulus produced different strain fields depending on its relative position with respect to the vessel lumen. The same phenomenon can also be seen experimentally for phantoms 2 and 3 in figure 7.

Following the spirit of Baldewsing *et al* (2008) and Li *et al* (2008), we successfully designed an original PFEM which constrains automatically and dynamically the inverse problem by progressively detecting and characterizing the mechanical properties of all plaque constituents. With regard to previous approaches, four major advantages can be stated. Our PFEM (1) highlights and adjusts automatically the shapes of all plaque heterogeneities without the help of any initial contour guesses as proposed by Baldewsing *et al* (2006), (2) appears to be sensitive to low strain amplitude and therefore is able to detect and characterize deep intraplaque soft atheromatous cores, (3) is able to reconstruct the modulogram of heterogeneous plaques with several soft inclusions using a procedure which takes into account mechanical interactions between the different plaque heterogeneities, and (4) satisfactorily computes the modulogram of any complex plaque by considering a high number of pre-conditioning regions, if required.

4.2. Characterization of lipid-rich plaque morphologies

4.2.1. Performance of our algorithm to detect complex plaque morphologies. The MST procedure can be seen as an essential step of the iMOD algorithm since it allowed a fast reconstruction of the intraplaque elasticity map. Indeed, for the vessel phantom mimicking a healthy coronary artery and phantoms with only one soft inclusion mimicking a necrotic core (figures 7 and 9, phantoms 1 and 2), the combined MST-DWS procedure was able to spatially constrain the inverse problem to a few numbers of pre-conditioning regions (close to 4). Note that for similar vulnerable plaques with a thin fibrous cap and one necrotic core, the algorithm of Baldewsing *et al* (2006) necessitated to guess the initial shape of the soft inclusion and moreover used approximately five additional geometric parameters to adjust the contours of the lipid inclusion. As the geometry of the necrotic core was directly and automatically identified by the MST-DWS procedure, the optimization of its shape was not necessary. In addition, our modulography algorithm iMOD appeared to be efficient in cases of plaques with two necrotic cores (figures 7 and 9, phantom 3) in which the mechanical interactions between the two inclusions were successfully taken into account. This constitutes

another major advantage of our approach since *in vivo* coronary plaques are expected to be often heterogeneous (Virmani *et al* 2000).

4.2.2. Performance of our algorithm to detect vulnerable plaques. The high values of the positive predictive and sensitivity indices obtained in the simulation and *in vitro* studies (table 1) demonstrate clearly that the proposed algorithm combining the strain estimator LSME, the pre-conditioning segmentation MST and the dynamic segmentation DWS procedures was reliable enough to detect simultaneously and accurately the morphologies of all plaque constituents.

As depicted in table 1 and figures 5–7, our procedure was able to estimate satisfactorily the $Core_{area}$ amplitude and Cap_{thick} larger than approximately $300\ \mu\text{m}$. A good quantification of these two morphological parameters is necessary since they represent the two most important geometrical indices used by cardiologists to predict plaque vulnerability (Naghavi *et al* 2003). By performing simulations of IVUS images with Field II, we found a mean relative Cap_{thick} error ranging from -72.3% (table 1, plaque 2) to 1.3% (table 1, plaque 7). For real IVUS images acquired *in vitro*, the relative Cap_{thick} error was slightly smaller (between -52.7% and 2.8%).

4.2.3. Reliability of our algorithm to reconstruct the elasticity map. By comparing Young's moduli identified by our algorithm with those measured by the compression tests (DMA) for the soft (one-cycle) and hard (six-cycle) PVA-C media, one can appreciate the performance of the proposed algorithm to identify the elasticity of the two media (table 1). Interestingly, modulograms obtained with phantom 3 showed clearly an increase of the internal layer's stiffness with pressure loading (see figure 9). We found that strain hardening effect was partly responsible for such variation. Indeed, experimental investigations performed on the six cycles (hard) and one cycle (soft) PVA-C media to characterize their nonlinear mechanical properties (figures 8(B) and 10) showed a significant increase of Young's modulus with strain amplitude. Note that the nonlinear behavior of the PVA-C gel was also highlighted by other experimental studies (Mori *et al* 1997, Wan *et al* 2002, Millon *et al* 2006, Pazos *et al* 2009). Such behavior explains why layers or sites with high compressive strains could appear stiffer in our vessel phantom modulograms.

To understand the origin of the bias on the soft inclusion's stiffness (table 1), one has to recall that the objective function implemented in the optimization procedure was computed from the experimental LSME radial strain field. Therefore, since the segmentation procedure may provide an estimated boundary between soft and stiff regions that is outside the soft inclusion contour, i.e. in the fibrous cap region, the algorithm tends to match the strain field of a rigid border with the guess of a soft material. As a global result of this boundary perturbation and kind of averaging, the soft inclusion's stiffness could be overestimated.

4.3. Study limitations

Some limitations deserve to be pointed out at this stage of our developments, even if the present study does highlight original and potentially promising concepts for improving VP detection.

- (1) The proposed algorithm underestimates the dimension of the fibrous cap for vulnerable plaques with Cap_{thick} smaller than approximately $300\ \mu\text{m}$ (table 1). In spite of the fact that this underestimation may result in a safer diagnosis of plaque vulnerability (i.e. false positives) (Ohayon *et al* 2008), this remains a limitation with regard to the accuracy of the

technique. Such errors made on the estimation of this morphological parameter are related to the features of LSME elastograms. Indeed, when using theoretical strain elastograms, iMOD satisfactorily estimated the Cap_{thick} value with a maximum absolute error of $32.5 \mu\text{m}$ (plaques 1 to 7, see figure 6(A)). Additional studies deserve to be performed in the future to investigate and improve the bias of our LSME for plaques with thin fibrous caps.

- (2) Our structural analysis was not performed in three dimensions but in two dimensions, assuming the plane strain condition. This could be a major limitation for *in vivo* studies, since the necrotic core length may be an important geometrical factor affecting the stability of a vulnerable plaque. However, the plane strain assumption we retained for our *in vitro* study is supported by considering that all manufactured phantom vessels had similar cross-sectional morphologies. Therefore, assuming a plane strain state means that we considered 3D phantom vessel geometries in which (i) neighboring cross-sectional morphologies remained similar, (ii) plaque length was large compared to the plaque radial dimension, and (iii) measurements were performed far from the vessel extremities to avoid all edge effects due to vessel attachments.
- (3) Such elasticity maps could be computed with a reasonable calculation time (close to 7 min with a PC with 4 cores of 3.2 GHz each and 8 Go of RAM) as far as the number of pre-conditioning regions remained smaller than approximately 15. Nevertheless, the calculations become very time consuming for high definition reconstruction elasticity maps (close to 3 h for approximately 150 pre-conditioning regions). Therefore, more efficient mathematical optimization algorithms could be selected (Avril *et al* 2008, Guo *et al* 2008, Ou *et al* 2008), which would decrease significantly the calculation time.

4.4. Potential clinical implications

Acute coronary syndromes are caused by an occlusion of the lumen by thrombi detaching from the lacerated vessel wall (Fuster *et al* 2005). There are several major mechanisms causing plaque disruption, including plaque erosion (Fuster *et al* 2005, Virmani *et al* 2006), tissue degradation due to macrophage infiltrations (Fuster *et al* 2005, Koenig 2001, Naghavi *et al* 2003) and biological activities responsible for the cellular inflammatory reaction (Fuster *et al* 2005, Arroyo and Lee 1999, Tedgui and Mallat 2006). Only *in vivo* imaging techniques could allow a better understanding of the evolution of plaque composition and morphology during arterial remodeling and grow process. The instability of a VP is mainly caused by the large mechanical stress that will develop in the thinnest part of the fibrous cap. It has been shown that this peak cap stress amplitude—a biomechanical predictor of plaque rupture—varies exponentially not only with Cap_{thick} but also with Young's modulus of the necrotic core (Finet *et al* 2004). Several animal and clinical studies conducted to analyze the structural variation in the fibrous cap and necrotic core demonstrated that statin treatment enhances plaque stability (Libby *et al* 2002). This shows how very slight structural changes can tilt a VP from stability to instability or vice versa. Such small changes may either 'precipitate' rupture or, conversely, 'stabilize' a vulnerable plaque. The *in vivo* use of the proposed LSME-iMOD imaging method may allow studying the evolution of the mechanical stability of atherosclerotic plaques. Additionally, the proposed method may allow elucidating why during the first few weeks to months of statin therapy vulnerable plaques tend to become more stable. This may likely be attributed to changes in the mechanical properties of plaque constituents, namely the hardening of the necrotic core, as suggested by FE simulations (Finet *et al* 2004).

Acknowledgments

The authors thank Professor Denis Favier (L3SR Laboratory, Grenoble, France) for the DMA experiment. Acknowledgements are also addressed to Dr Jérémie Fromageau and Mr Cédric Schmitt of the Laboratory of Biorheology and Medical Ultrasonics, University of Montreal Hospital Research Center, for their experimental supports during *in vitro* phantom experiments. Grant supports were provided by the Agence Nationale de la Recherche (ANR), France (ATHEBIOMECH project 06-BLAN-0263), and by the collaborative health research joint program of the Natural Sciences and Engineering Research Council of Canada (NSERC 323405-06) and Canadian Institutes of Health Research (CIHR CPG-80085). This research is now supported by a joint international program of the ANR (MELANII project 09-BLAN-0423) and NSERC strategic grant STPGP-381136-09. Financial support was also provided by a post-doctoral appointment (S Le Floc'h) from a valorization research program of the University Joseph Fourier (UJF), France, in partnership with Floralis-France. Funding was also obtained from the Rhône-Alpes (France) research cluster (I3M: Medical Images and Multiscale Models).

References

- Arroyo L H and Lee R T 1999 Mechanisms of plaque rupture: mechanical and biologic interactions *Cardiovasc. Res.* **41** 369–75
- Avril S, Huntley J M, Pierron F and Steele D D 2008 3D heterogeneous stiffness reconstruction using MRI and the virtual fields method *Exp. Mech.* **48** 479–94
- Baldewsing R A, Mastik F, Schaar J A, Serruys P W and van der Steen A F 2005 Robustness of reconstructing the Young's modulus distribution of vulnerable atherosclerotic plaques using a parametric plaque model *Ultrasound Med. Biol.* **31** 1631–45
- Baldewsing R A, Mastik F, Schaar J A, Serruys P W and van der Steen A F 2006 Young's modulus reconstruction of vulnerable atherosclerotic plaque components using deformable curves *Ultrasound Med. Biol.* **32** 201–10
- Baldewsing R A, Danilouchkine M G, Mastik F, Schaar J A, Serruys P W and van der Steen A F 2008 An inverse method for imaging the local elasticity of atherosclerotic coronary plaques *IEEE Trans. Inf. Technol. Biomed.* **12** 277–89
- Barbone P E and Bamber J C 2002 Quantitative elasticity imaging: what can and cannot be inferred from strain images *Phys. Med. Biol.* **47** 2147–64
- Beattie D, Xu C, Vito R, Glagov S and Whang M C 1998 Mechanical analysis of heterogeneous, atherosclerotic human aorta *J. Biomech. Eng.* **120** 602–7
- Briley-Saebo K C, Mulder W J, Mani V, Hyafil F, Amirbekian V, Aguinaldo J G, Fisher E A and Fayad Z A 2007 Magnetic resonance imaging of vulnerable atherosclerotic plaques: current imaging strategies and molecular imaging probes *J. Magn. Reson. Imaging* **26** 460–79
- Carlier S G and Tanaka K 2006 Studying coronary plaque regression with IVUS: a critical review of recent studies *J. Interv. Cardiol.* **19** 11–5
- Chandran K B, Mun J H, Choi K K, Chen J S, Hamilton A, Nagaraj A and McPherson D D 2003 A method for *in vivo* analysis for regional arterial wall material property alterations with atherosclerosis: preliminary results *Med. Eng. Phys.* **25** 289–98
- Cheng G C, Loree H M, Kamm R D, Fishbein M C and Lee R T 1993 Distribution of circumferential stress in ruptured and stable atherosclerotic lesions. A structural analysis with histopathological correlation *Circulation* **87** 1179–87
- Cimrman R and Rohan E 2010 On the identification of the arterial model parameters from experiments applicable 'in vivo' *Math. Comput. Simul.* **80** 1232–45
- de Korte C L, Carlier S G, Mastik F, Doyley M M, van der Steen A F, Serruys P W and Bom N 2002 Morphological and mechanical information of coronary arteries obtained with intravascular elastography: feasibility study *in vivo Eur. Heart J.* **23** 405–13
- Fayad Z A, Fuster V, Nikolaou K and Becker C 2002 Computed tomography and magnetic resonance imaging for noninvasive coronary angiography and plaque imaging: current and potential future concepts *Circulation* **106** 2026–34

- Fehrenbach J, Masmoudi M, Souchon R and Trompette P 2006 Detection of small inclusions by elastography *Inverse Problems* **22** 1055
- Finet G, Ohayon J and Rioufol G 2004 Biomechanical interaction between cap thickness, lipid core composition and blood pressure in vulnerable coronary plaque: impact on stability or instability *Coron. Artery Dis.* **15** 13–20
- Fromageau J 2003 Estimation itérative du déplacement et de la déformation pour l'imagerie ultrasonore de l'élasticité des tissus biologiques. Application à l'échographie endovasculaire *PhD Thesis* Institut National des Sciences Appliquées de Lyon—France
- Fromageau J, Gennisson J L, Schmitt C, Maurice R L, Mongrain R and Cloutier G 2007 Estimation of polyvinyl alcohol cryogel mechanical properties with four ultrasound elastography methods and comparison with gold standard testings *IEEE Trans. Ultrason. Ferroelectr. Freq. Control* **54** 498–509
- Fuster V, Moreno P R, Fayad Z A, Corti R and Badimon J J 2005 Atherothrombosis and high-risk plaque: part I: evolving concepts *J. Am. Coll. Cardiol.* **46** 937–54
- Gill P E, Murray W and Saunders M A 2005 SNOPT: an SQP algorithm for large-scale constrained optimization *SIAM Rev.* **47** 99–131
- Guo Z, You S, Wan X and Bicanic N 2008 A FEM-based direct method for material reconstruction inverse problem in soft tissue elastography *Comput. Struct.* (in press)
- Jang I K *et al* 2002 Visualization of coronary atherosclerotic plaques in patients using optical coherence tomography: comparison with intravascular ultrasound *J. Am. Coll. Cardiol.* **39** 604–9
- Jensen J A and Svendsen N B 1992 Calculation of pressure fields from arbitrarily shaped, apodized, and excited ultrasound transducers *IEEE Trans. Ultrason. Ferroelectr. Freq. Control.* **39** 262–7
- Kanai H, Hasegawa H, Ichiki M, Tezuka F and Koiwa Y 2003 Elasticity imaging of atheroma with transcutaneous ultrasound: preliminary study *Circulation* **107** 3018–21
- Karimi R, Zhu T, Bouma B E and Mofrad M R 2008 Estimation of nonlinear mechanical properties of vascular tissues via elastography *Cardiovasc. Eng.* **8** 191–202
- Khalil A S, Bouma B E and Kaazempur Mofrad M R 2006 A combined FEM/genetic algorithm for vascular soft tissue elasticity estimation *Cardiovasc. Eng.* **6** 93–102
- Kim K, Weitzel W F, Rubin J M, Xie H, Chen X and O'Donnell M 2004 Vascular intramural strain imaging using arterial pressure equalization *Ultrasound Med. Biol.* **30** 761–71
- Koenig W 2001 Inflammation and coronary heart disease: an overview *Cardiol. Rev.* **9** 31–5
- Kubo T *et al* 2007 Assessment of culprit lesion morphology in acute myocardial infarction: ability of optical coherence tomography compared with intravascular ultrasound and coronary angiography *J. Am. Coll. Cardiol.* **50** 933–9
- Le Floc'h S, Ohayon J, Tracqui P, Finet G, Gharib A M, Maurice R L, Cloutier G and Pettigrew R I 2009 Vulnerable atherosclerotic plaque elasticity reconstruction based on a segmentation-driven optimization procedure using strain measurements: theoretical framework *IEEE Trans. Med. Imaging* **28** 1126–37
- Levner I and Zhang H 2007 Classification-driven watershed segmentation *IEEE Trans. Image Process.* **16** 1437–45
- Li J, Cui Y, Kadour M and Noble J A 2008 Elasticity reconstruction from displacement and confidence measures of a multi-compressed ultrasound RF sequence *IEEE Trans. Ultrason. Ferroelectr. Freq. Control.* **55** 319–26
- Libby P 2001 Current concepts of the pathogenesis of the acute coronary syndromes *Circulation* **104** 365–72
- Libby P, Ridker P M and Maseri A 2002 Inflammation and atherosclerosis *Circulation* **105** 1135–43
- Loree H M, Kamm R D, Stringfellow R G and Lee R T 1992 Effects of fibrous cap thickness on peak circumferential stress in model atherosclerotic vessels *Circ. Res.* **71** 850–8
- Maurice R L, Brusseau E, Finet G and Cloutier G 2005a On the potential of the Lagrangian speckle model estimator to characterize atherosclerotic plaques in endovascular elastography: *in vitro* experiments using an excised human carotid artery *Ultrasound Med. Biol.* **31** 85–91
- Maurice R L, Fromageau J, Brusseau E, Finet G, Rioufol G and Cloutier G 2007 On the potential of the Lagrangian estimator for endovascular ultrasound elastography: *in vivo* human coronary artery study *Ultrasound Med. Biol.* **33** 1199–205
- Maurice R L, Ohayon J, Finet G and Cloutier G 2004 Adapting the Lagrangian speckle model estimator for endovascular elastography: theory and validation with simulated radio-frequency data *J. Acoust. Soc. Am.* **116** 1276–86
- Maurice R L, Daronat M, Ohayon J, Stoyanova E, Foster F S and Cloutier G 2005b Non-invasive high-frequency vascular ultrasound elastography *Phys. Med. Biol.* **50** 1611–28
- Millon L E, Mohammadi H and Wan W K 2006 Anisotropic polyvinyl alcohol hydrogel for cardiovascular applications *J. Biomed. Mater. Res. B Appl. Biomater.* **79** 305–11
- Mori Y, Tokura H and Yoshikawa M 1997 Properties of hydrogels synthesized by freezing and thawing aqueous polyvinyl alcohol solutions and their applications *J. Mater. Sci.* **32** 491–6
- Naghavi M *et al* 2003 From vulnerable plaque to vulnerable patient: a call for new definitions and risk assessment strategies: part I *Circulation* **108** 1664–72

- Ohayon J, Finet G, Gharib A M, Herzka D A, Tracqui P, Heroux J, Rioufol G, Kotys M S, Elagha A and Pettigrew R I 2008 Necrotic core thickness and positive arterial remodeling index: emergent biomechanical factors for evaluating the risk of plaque rupture *Am. J. Phys. Heart Circ. Phys.* **295** H717–27
- Ohayon J, Teppaz P, Finet G and Rioufol G 2001 *In vivo* prediction of human coronary plaque rupture location using intravascular ultrasound and the finite element method *Coron. Artery Dis.* **12** 655–63
- Ou J J, Ong R E, Yankeelov T E and Miga M I 2008 Evaluation of 3D modality-independent elastography for breast imaging: a simulation study *Phys. Med. Biol.* **53** 147–63
- Pazos V, Mongrain R and Tardif J C 2009 Polyvinyl alcohol cryogel: optimizing the parameters of cryogenic treatment using hyperelastic models *J. Mech. Behav. Biomed. Mater.* **2** 542–9
- Pazos V, Mongrain R and Tardif J C 2010 Mechanical characterization of atherosclerotic arteries using finite element modeling: feasibility study on mock arteries *IEEE Trans. Biomed. Eng.* **57** 1520–8
- Ramirez M D R, Ivanova P R, Mauri J and Pujol O 2004 Simulation model of intravascular ultrasound images *Medical Image Computing and Computer-Assisted Intervention MICCAI 2004 (France)*
- Rioufol G, Finet G, Ginon I, Andre-Fouet X, Rossi R, Vialle E, Desjoyaux E, Convert G, Huret J F and Tabib A 2002 Multiple atherosclerotic plaque rupture in acute coronary syndrome: a three-vessel intravascular ultrasound study *Circulation* **106** 804–8
- Roy Cardinal M H, Meunier J, Soulez G, Maurice R L, Therasse E and Cloutier G 2006 Intravascular ultrasound image segmentation: a three-dimensional fast-marching method based on gray level distributions *IEEE Trans. Med. Imaging* **25** 590–601
- Shah P K 1998 Plaque size, vessel size and plaque vulnerability: bigger may not be better *J. Am. Coll. Cardiol.* **32** 663–4
- Soualmi L, Bertrand M, Mongrain R and Tardif J C 1997 Forward and inverse problems in endovascular elastography *Acoustical Imaging* (New York: Plenum)
- Sumi C and Nakayama K 1998 A robust numerical solution to reconstruct a globally relative shear modulus distribution from strain measurements *IEEE Trans. Med. Imaging* **17** 419–28
- Tearney G J *et al* 2008 Three-dimensional coronary artery microscopy by intracoronary optical frequency domain imaging *JACC Cardiovasc. Imaging* **1** 752–61
- Tedgui A and Mallat Z 2006 Cytokines in atherosclerosis: pathogenic and regulatory pathways *Phys. Rev.* **86** 515–81
- Vengrenyuk Y, Carlier S, Xanthos S, Cardoso L, Ganatos P, Virmani R, Einav S, Gilchrist L and Weinbaum S 2006 A hypothesis for vulnerable plaque rupture due to stress-induced debonding around cellular microcalcifications in thin fibrous caps *Proc. Natl Acad. Sci. USA* **103** 14678–83
- Virmani R, Burke A P, Farb A and Kolodgie F D 2006 Pathology of the vulnerable plaque *J. Am. Coll. Cardiol.* **47** C13–8
- Virmani R, Kolodgie F D, Burke A P, Farb A and Schwartz S M 2000 Lessons from sudden coronary death: a comprehensive morphological classification scheme for atherosclerotic lesions *Arterioscler. Thromb. Vasc. Biol.* **20** 1262–75
- Vonesh M J, Cho C H, Pinto J V Jr, Kane B J, Lee D S, Roth S I, Chandran K B and McPherson D D 1997 Regional vascular mechanical properties by 3-D intravascular ultrasound with finite-element analysis *Am. J. Phys.* **272** H425–37
- Vorp D A, Rajagopal K R, Smolinski P J and Borovetz H S 1995 Identification of elastic properties of homogeneous, orthotropic vascular segments in distension *J. Biomech.* **28** 501–12
- Wan M, Li Y, Li J, Cui Y and Zhou X 2001 Strain imaging and elasticity reconstruction of arteries based on intravascular ultrasound video images *IEEE Trans. Biomed. Eng.* **48** 116–20
- Wan W K, Campbell G, Zhang Z F, Hui A J and Boughner D R 2002 Optimizing the tensile properties of polyvinyl alcohol hydrogel for the construction of a bioprosthetic heart valve stent *J. Biomed. Mater. Res.* **63** 854–61